

RESEARCH

Open Access



Photothermal Fe₃O₄ nanoparticles induced immunogenic ferroptosis for synergistic colorectal cancer therapy

Yue Li^{1,2†}, Jia Chen^{1,5†}, Qi Xia¹, Jing Shang^{1,4}, Yujie He^{1,5}, Zhi Li¹, Yingying Chen^{1,2}, Feng Gao³, Xi Yu^{1,2*}, Zeting Yuan^{1,2,3,4*} and Peihao Yin^{1,4,5*}

Abstract

Photothermal therapy (PTT) is a promising non-invasive treatment that has shown great potential in eliminating tumors. It not only induces apoptosis of cancer cells but also triggers immunogenic cell death (ICD) which could activate the immune system against cancer. However, the immunosuppressive tumor microenvironment (TIME) poses a challenge to triggering strong immune responses with a single treatment, thus limiting the therapeutic effect of cancer immunotherapy. In this study, dual-targeted nano delivery system (GOx@FeNPs) combined with αPD-L1 immune checkpoint blocker could inhibit colorectal cancer (CRC) progression by mediating PTT, ferroptosis and anti-tumor immune response. Briefly, specific tumor delivery was achieved by the cyclic arginine glyceryl aspartate (cRGD) peptide and anisamide (AA) in GOx@FeNPs which not only had a good photothermal effect to realize PTT and induce ICD, but also could deplete glutathione (GSH) and catalyze the production of reactive oxygen species (ROS) from endogenous H₂O₂. All these accelerated the Fenton reaction and augmented the process of PTT-induced ICD. Thus, a large amount of tumor specific antigen was released to stimulate the maturation of dendritic cells (DCs) in lymph nodes and enhance the infiltration of CD8⁺ T cells in tumor. At the same time, the combination with αPD-L1 has favorable synergistic effectiveness against CRC with tumor inhibition rate over 90%. Furthermore, GOx@FeNPs had good magnetic resonance imaging (MRI) capability under T2-weighting owing to the presence of Fe³⁺, which is favorable for integrated diagnosis and treatment systems of CRC. By constructing a dual-targeted GOx@FeNPs nanoplatfrom, PTT synergistically combined with ferroptosis was realized to improve the immunotherapeutic effect, providing a new approach for CRC immunotherapy.

Keywords Photothermal therapy, Ferroptosis, ICD, Immunotherapy, CRC

[†]Yue Li and Jia Chen contributed equally to this work.

*Correspondence:

Xi Yu
495003741@qq.com
Zeting Yuan
yuan340202@163.com
Peihao Yin
yinpeihao@shutcm.edu.cn

¹Interventional Cancer Institute of Chinese Integrative Medicine & Putuo Hospital, Shanghai University of Traditional Chinese Medicine, Shanghai 200062, China

²Central Laboratory, Putuo Hospital, Shanghai University of Traditional Chinese Medicine, Shanghai 200062, China

³Department of Pharmaceutics, School of Pharmacy, East China University of Science and Technology, Shanghai 200237, China

⁴Shanghai Putuo Central School of Clinical Medicine, Anhui Medical University, Shanghai 200062, China

⁵School of Medicine and Life Sciences, Chengdu University of Traditional Chinese Medicine, Chengdu 610075, China



Introduction

Cancer immunotherapy, represented by PD-1/PD-L1 immune checkpoint blockade (ICB), has emerged as one of the major strategies for colorectal cancer (CRC) in recent years [1]. It not only prolongs the survival of patients, but also has a high immune response in patients with metastatic cancer [2]. However, most CRC patients with mismatch repair-proficient (pMMR) and microsatellite stability (MSS) have a poor immunologic response [3–5]. The main reason is that low immunogenicity of tumor cells prevents antigen-presenting cells such as dendritic cells (DCs) from capturing and presenting the tumor antigens to cytotoxic T lymphocytes (CTLs). As a result, CTLs are unable to infiltrate the tumor. Therefore, the key to enhancing PD-1/PD-L1 therapy for CRC lies in effectively inducing immunogenicity and breaking the immunosuppressive tumor microenvironment (TIME).

A feasible approach to trigger an immune response is to induce immunogenic cell death (ICD) of cancerous cells [6, 7], where various damage-associated molecular patterns (DAMPs), such as calreticulin (CRT), high mobility group protein (HMGB1), and adenosine triphosphate (ATP) are released [8]. A number of researches have shown that photothermal therapy (PTT) can induce ICD by releasing tumor specific antigens [9–11]. PTT is a novel cancer treatment that involves converting light into heat through exogenous photothermal agents (PTA) under near-infrared light (NIR), which is becoming increasingly popular as a clinical choice for its controllable and non-invasive benefits [12–14]. Moreover, PTT can not only kill tumors directly, but also synergistically stimulates the immune response when combined with other therapeutic approaches, including the redistribution and activation of immune effector cells, the expression and secretion of cytokines, and transformation of memory T lymphocytes [15]. With the development of nanotechnology, photothermal nanomaterials-mediated PTT displays a promising application in tumor diagnosis and treatment when coupled with chemotherapy [16–20], radiotherapy [21–24], and photodynamic therapy [25–27], as it has a higher photothermal conversion rate and more precise tumor targeting when compared to conventional PTA [28, 29]. However, it's important to note that the immunogenicity of cell death induced by a single PTT is usually mild, which may be counterbalanced by the TIME.

To tackle the challenge, a synergistic approach can be employed by combining ferroptosis which is a new regulated form of cell death distinct from apoptosis, necrosis and autophagy, showing unique benefits in antitumor therapy [30–32]. It is caused by excessive accumulation of intracellular iron and leads to the inactivation of the glutathione (GSH) antioxidant system [33, 34], followed by the accumulation of lipid peroxides (LPO) and ultimately

causing cellular damage [35–37]. Interestingly, the induction of ferroptosis is always accompanied by the release of tumor antigens and DAMPs, which trigger tumor specific immune responses [38–40]. Therefore, in combination with PTT, it is hoped that tumor immunogenicity can be boosted, thus effectively activating the anti-tumor immune response [41–43]. However, common small-molecule ferroptosis inducers such as erastin, RSL3 and FeCl_2 generally suffer from easy metabolism and poor selectivity in vivo, which limits their applications [44, 45].

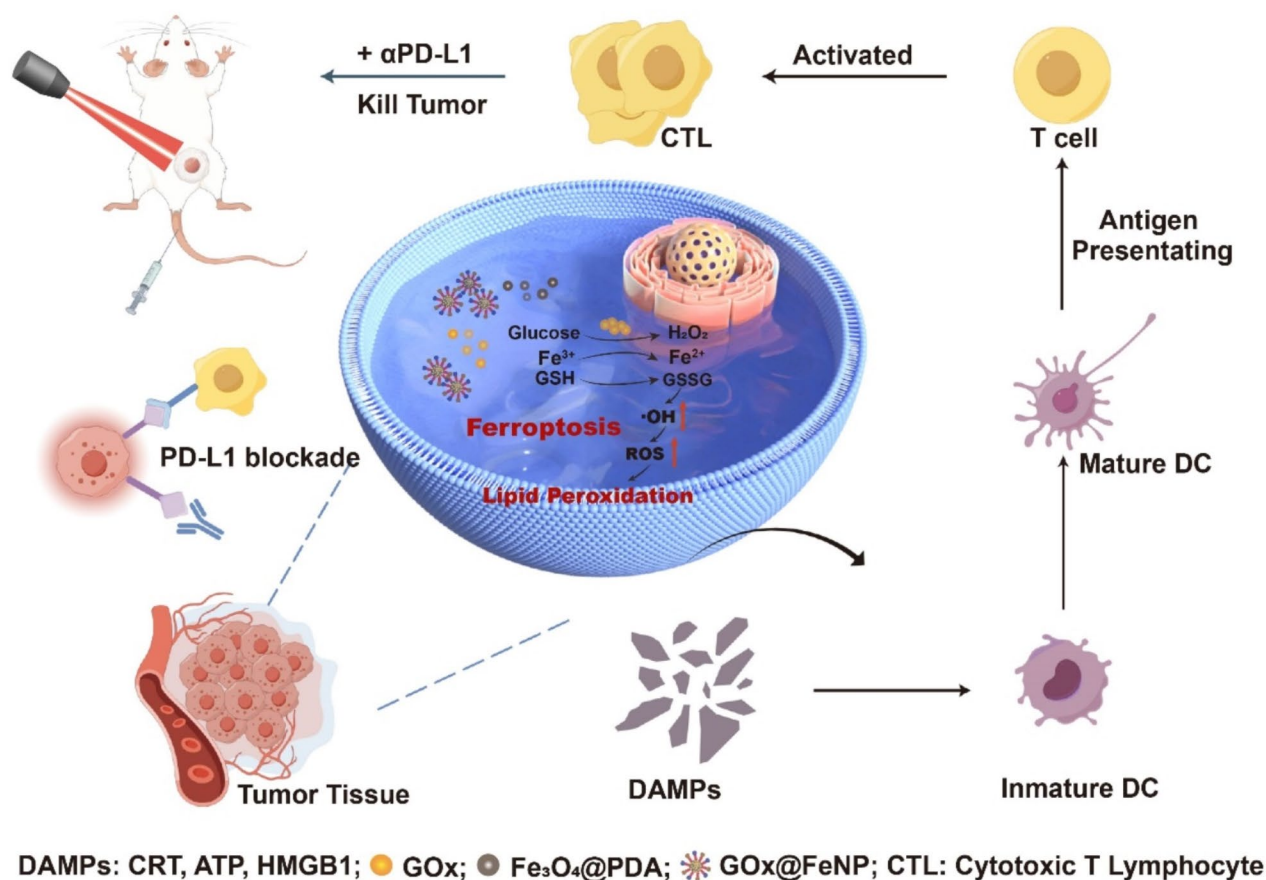
Extensive researches have been conducted in recent years to investigate the application of nano-delivery systems for treating CRC owing to their superior targeting [46], functionalizable modifications, and biodegradability [47–51]. Thus, Fe_3O_4 nanoparticles, approved by the U.S. Food and Drug Administration (FDA) for clinical studies, were chosen as basic material due to the good biocompatibility, photothermal conversion properties, magnetic responsiveness, and other desirable features [52]. To prevent Fe_3O_4 nanoparticles from self-aggregating, polydopamine (PDA) with photothermal properties was chosen to be post-modified to obtain Fe_3O_4 @PDA nanoparticles [53, 54].

Inspired by this, our work aimed to improve the tumor targeting ability of Fe_3O_4 @PDA nanoparticles by using the cyclic arginine glycyl aspartate (cRGD) peptide and anisamide (AA). By introducing glucose oxidase (GOx), the Fe^{2+} -mediated Fenton reaction was further accelerated which enhanced cellular ferroptosis. As a result, a nanotherapeutic platform Fe_3O_4 @PDA-PEG-cRGD-AA@GOx (abbreviated as GOx@FeNPs) with dual targeting, photothermal conversion, ferroptosis induction, and magnetic resonance imaging (MRI) was obtained. Once GOx@FeNPs were actively targeted to the tumor site, the individual components were thermally liberated under NIR laser. The released Fe_3O_4 @PDA exerts photothermal conversion properties to induce tumor cell apoptosis and ICD. At the same time, Fe^{3+} was reduced to Fe^{2+} in the presence of endogenous GSH and then reacted with H_2O_2 from GOx-catalyzed glucose in a Fenton reaction, leading to the accumulation of LPO and ultimately ferroptosis. The massive release of tumor specific antigens and DAMPs resulted from ICD and ferroptosis promoted the maturation of DCs and the infiltration of CTLs, triggering an effective systemic anti-tumor immune response and inhibiting tumor growth. In addition, GOx@FeNPs can be combined with the α PD-L1 to further enhance immunotherapeutic effect (Scheme 1).

Results and discussion

Preparation and characterization of dual-targeted Fe_3O_4 nanoparticles

The GOx@FeNPs nanoparticles (NPs) were designed and prepared based on our previous studies [53], and



Scheme 1 Schematic illustration of GOx@FeNPs-mediated PTT synergizing with ferroptosis by inducing ICD to improve colorectal cancer immunotherapy

the synthesis procedure was shown in Fig. 1A. First, Fe₃O₄@PDA NPs were prepared by self-aggregation of dopamine (DA) and Fe₃O₄ nanoparticles in an alkaline aqueous solution. Afterwards, NH₂-PEG-RGD and NH₂-PEG-AA were obtained separately by acylation reactions with cRGD and AA. Finally, Fe₃O₄@PDA reacted with the amino groups in NH₂-PEG-RGD and NH₂-PEG-AA through a Schiff base reaction, effectively attaching the two targets to the nanoparticle surfaces, and eventually forming Fe₃O₄@PDA-PEG-cRGD-AA NPs. Then we chose GOx to catalyze the Fenton reaction, which was loaded onto Fe₃O₄@PDA-PEG-cRGD-AA NPs via π - π stacking to finally obtain GOx@FeNPs. As shown in Fig. 1B, GOx@FeNPs had a typical core-shell structure with well dispersion and the average particle size is around 150 nm (Figure S1). Figure S2 demonstrated that the average zeta potential of the GOx@FeNPs was -23 mV, indicating its good stability. To examine the photothermal properties, heating curves of GOx@FeNPs solution with different concentrations (0, 25, 50, and 100 μ g/mL) were recorded under irradiation of 808 nm NIR laser (1 W/cm², 5 min). The results showed that GOx@FeNPs

exhibited both time and concentration-dependent photothermal behaviors. The temperature of 100 μ g/mL samples increased from 26.1 °C to 51.2 °C under irradiation, while the PBS was only increased from 26.6 °C to 31.1 °C under the same condition (Fig. 2D and E). Moreover, the heating and cooling cycle experiments also showed that the temperature of GOx@FeNPs could remain at 48 °C stably after 5 cycles, demonstrating a good photothermal stability (Fig. 1C). The above results proved that GOx@FeNPs with good photothermal conversion properties and photothermal stability under NIR irradiation were prepared successfully.

Anti-tumor activity of GOx@FeNPs in vitro

The effective uptake of nanoparticles into tumor cells is crucial for their anti-tumor effects. Thus, green fluorescent dye coumarin 6 (Ce6) was used to label GOx@FeNPs for assessing the cellular uptake by CT26 cells under a confocal laser scanning microscopy (CLSM). As shown in Fig. 3A, the fluorescence intensity reached the maximum level after 4 h, showing a time-dependent trend. Due to the introduction of the dual-targets, the cellular uptake

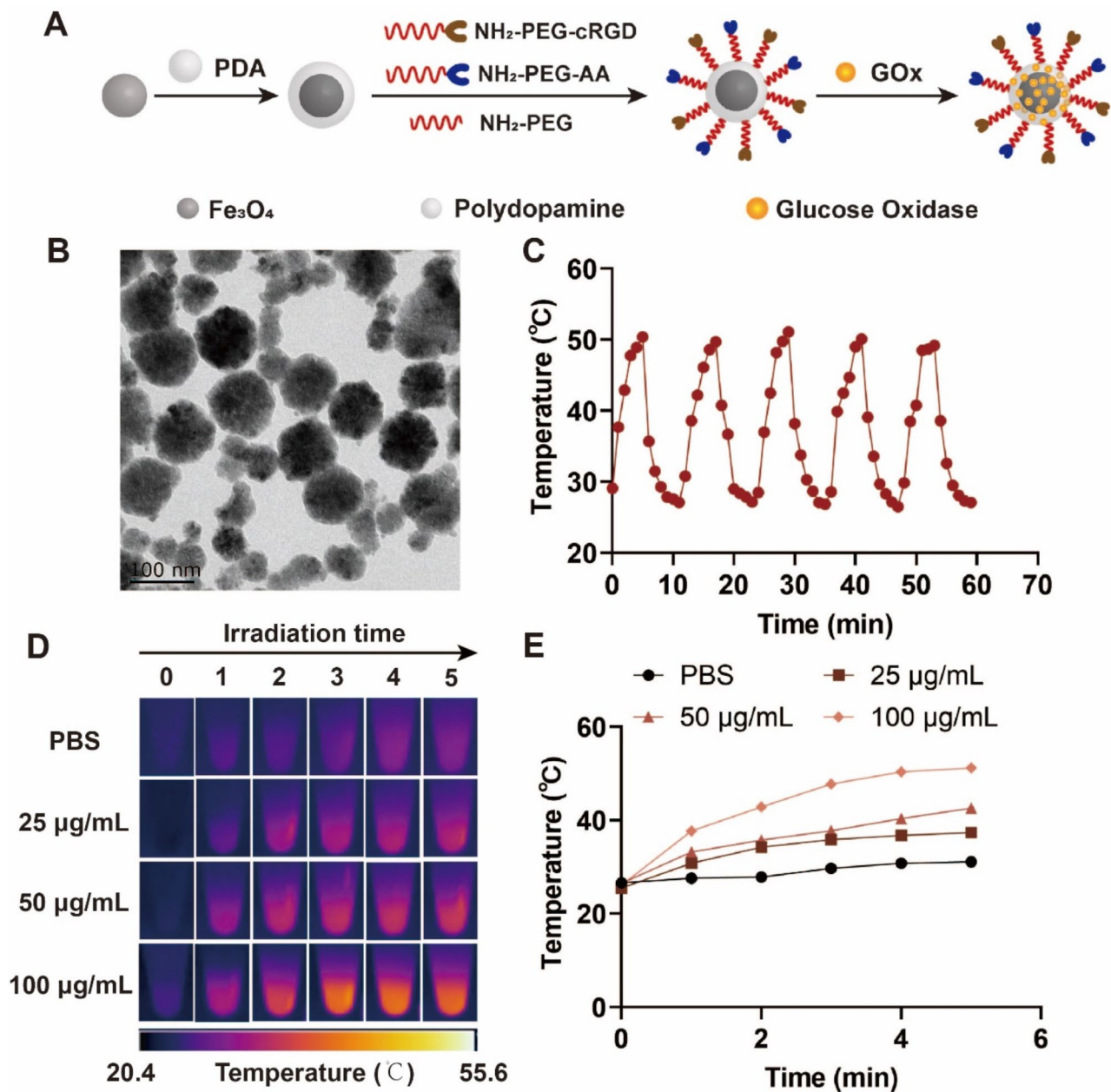


Fig. 1 Preparation and photothermal performance characterization of GOx@FeNPs. **(A)** Schematic of the synthesis of GOx@FeNPs. **(B)** TEM images of GOx@FeNPs (scale bar = 100 nm). **(C)** Heating and cooling curve of the GOx@FeNPs with the laser turned on and off for 5 cycles. **(D)** Infrared thermal imaging of GOx@FeNPs suspensions with different concentrations under constant NIR laser. **(E)** Temperature variation curves of GOx@FeNPs suspension of NIR laser

time was shortened by 2 h compared with that in the literature [33]. Therefore, 4 h was chosen as the incubation time of GOx@FeNPs for all subsequent experiments. To verify that the modified tumor cell uptake property was owing to the synergistic effect of cRGD-integrin $\alpha\beta_3$ receptor on the tumor neovasculature [55] and the AA- σ_1 receptor on the surface of fibroblasts [56], CT26 cells were pretreated with free RGD peptide and AA respectively for 30 min (Figure S3). As anticipated, the cellular

uptake was significantly decreased due to the competitive binding of excess RGD peptide and AA to cell surface receptors. All the above experiments demonstrated that the introduction of cRGD and AA ensured the excellent tumor-targeted capacity of GOx@FeNPs.

In order to test the anti-tumor effect of GOx@FeNPs in vitro, CCK-8 experiments of CT26 cells was conducted. Results showed that the cell survival rates were all above 90% without laser, which proved that GOx@

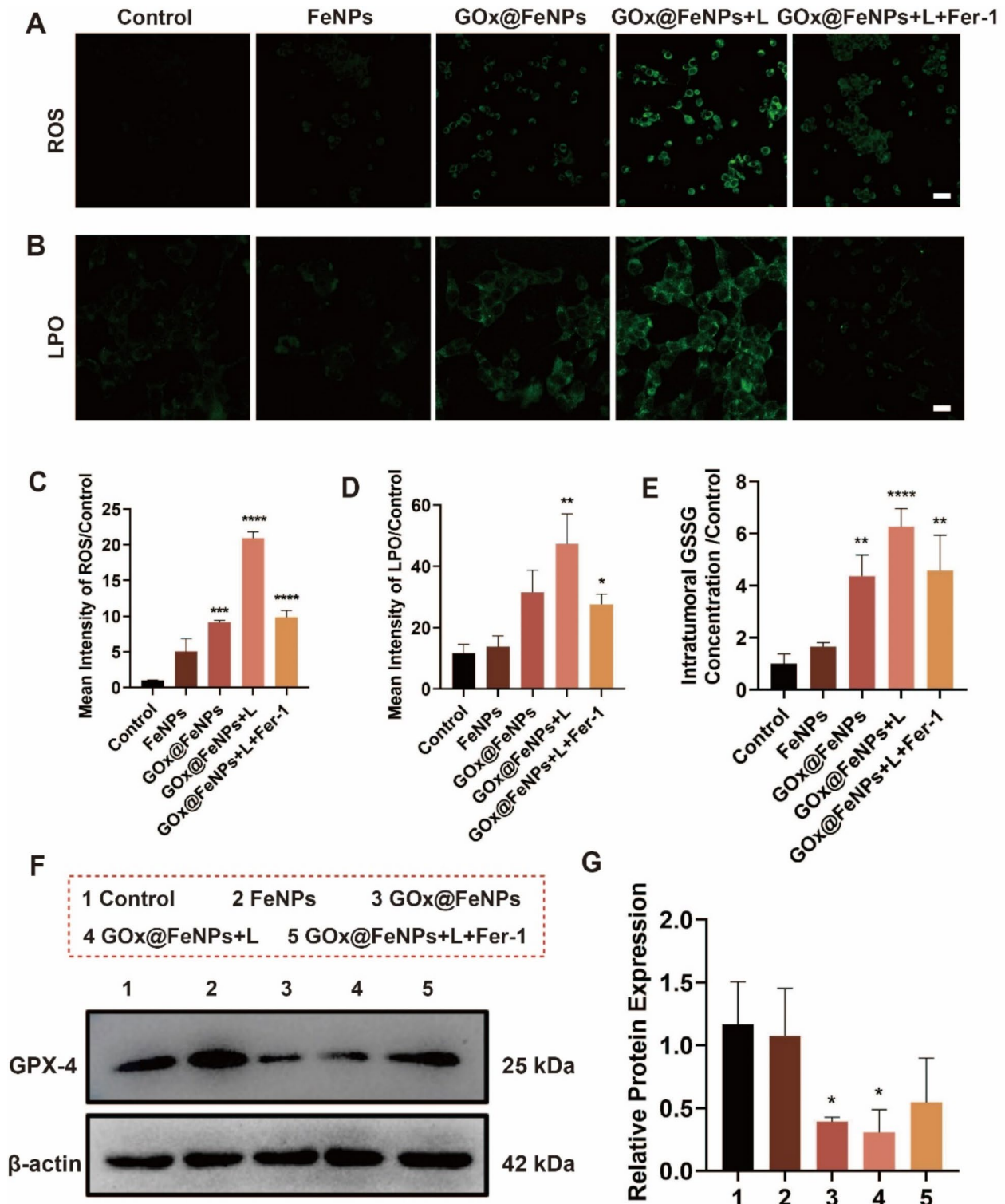


Fig. 2 Ferroptosis induced by GOx@FeNPs in vitro. **(A–B)** Fluorescence imaging of ROS and LPO in CT26 cells treated with Control, FeNPs, GOx@FeNPs, GOx@FeNPs+L, GOx@FeNPs+L+Fer-1, and **(C–D)** mean fluorescence intensity. Scale bar: 50 μ m, mean \pm SD; $n=3$. **(E)** Intracellular GSSG concentration in CT26 cells after different treatments, mean \pm SD; $n=3$. **(F)** The expression of GPX4 protein after different treatments was measured by western blotting and **(G)** quantitatively analyzed, mean \pm SD; $n=3$. * $p<0.05$, ** $p<0.01$, *** $p<0.001$, **** $p<0.0001$

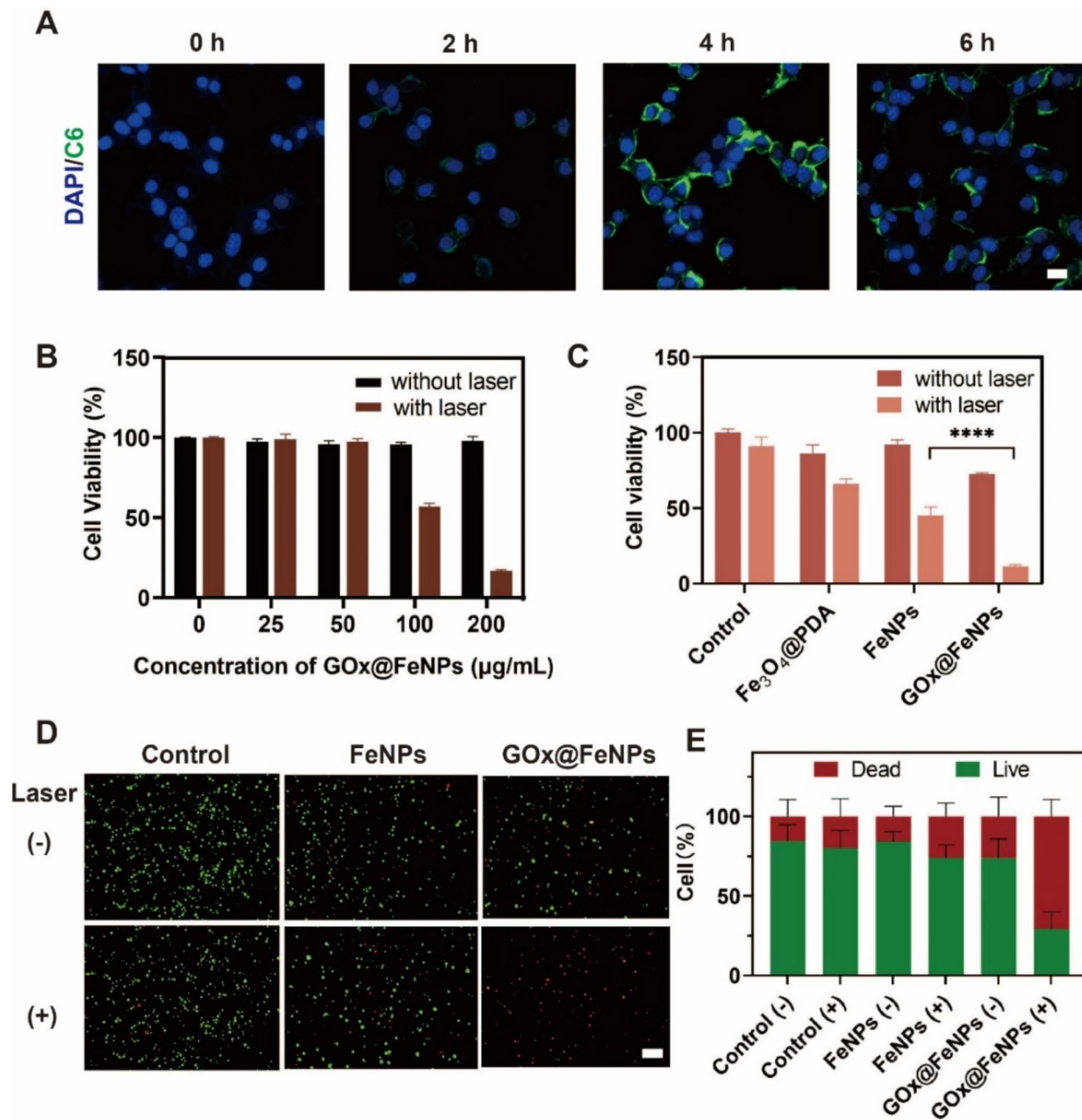


Fig. 3 Cellular uptake and anti-tumor proliferation in vitro. **(A)** The CLSM images of 0, 2, 4 and 6 h CT26 cells processed with Ce6-labeled GOx@FeNPs. (scale bar = 50 µm). **(B)** Viability of CT26 cells after treatment with different concentrations of GOx@FeNPs for 24 h. **(C)** Viability of CT26 cells after treatment with different nanoformulations, concentration of 100 ng/mL in all groups. **(D)** Fluorescence images of CT26 cells after double staining with calcein-AM/PI after treatment of FeNPs and GOx@FeNPs with or without laser. scale bar = 100 µm. **(E)** Quantitative fluorescence statistic plot of CT26 cell death levels after different formulations, green and red colors indicate live and dead cells, respectively (mean ± SD; n = 3). **p* < 0.05, ***p* < 0.01, ****p* < 0.001, *****p* < 0.0001

FeNPs had a good biosafety. However, there was an obvious cytotoxicity with laser in a concentration-dependent manner (Fig. 3B). At the same time, to explain the impact of GOx on anti-tumor efficacy of Fe₃O₄@PDA, Fe₃O₄@PDA-PEG-RGD-AA NPs (FeNPs) and GOx@FeNPs were compared in killing cancer cells. As shown in Fig. 3C, the FeNPs group exhibited stronger cytotoxicity than

the Fe₃O₄@PDA group under laser irradiation. This was attributed to better tumor-targeting performance after the introduction of dual-targeted cRGD peptide and AA. When loaded with GOx enzymes, the GOx@FeNPs group exhibited the strongest cytotoxicity. The cell viability was approximately 12% with laser, which was 20% lower than the reported nanoplateform with the same

strategy [16]. Even without laser, GOx@FeNPs group also showed about 70% cell viability versus more than 90% in the FeNPs group, suggesting GOx might accelerate cellular ferroptosis. The results demonstrated the prepared GOx@FeNPs could inhibit tumor proliferation via enhancing PTT synergized with ferroptosis. To further validate the cytotoxicity of the different formulations, the Calcein-AM/PI co-staining assay was performed. As shown in Fig. 3D and E, the number of dead cells (red fluorescence) in the GOx@FeNPs+L group was about 80%, which was significantly higher than that of other groups, proving its killing efficiency against CRC cells. Overall, these results confirmed the enhanced anti-tumor potential of tumor-targeted GOx@FeNPs with PTT and ferroptosis.

Ferroptosis of tumor cells induced by GOx@FeNPs in vitro

According to the Warburg effect, intracellular glucose can be converted to H_2O_2 by the GOx enzyme, which reacts with Fe^{2+} to produce $\bullet OH$, leading to the accumulation of lipid peroxides ultimately [57, 58]. This process is accompanied by GSH depletion, reactive oxygen species (ROS) production, downregulation of glutathione peroxidase 4 (GPX4) and excessive accumulation of LPO, which are all typical characteristics of ferroptosis. To prove that GOx@FeNPs could induce and accelerate ferroptosis, DCFH-DA and BODIPY^{581/591}-C11 were selected as fluorescent probes to investigate the expression of ROS and LPO by CLSM respectively (Fig. 2A and B). As similar to the control, the green fluorescence signal was barely visible in the FeNPs group. But the GOx@FeNPs group showed obvious signals, indicating the ferroptosis in FeNPs group was limited, while the addition of GOx promoted the production of ROS and LPO and accelerated the Fenton reaction and subsequent ferroptosis. Moreover, the fluorescence signal of the GOx@FeNPs+L group was increased by 2.3-fold and 1.5-fold for ROS and LPO respectively, compared with that of the GOx@FeNPs group without laser. (Figure 2C and D). However, the added ferroptosis inhibitor ferrostatin-1 (Fer-1) could rescue the oxidative stress level to some extent. Oxidized glutathione (GSSG), an oxidized form of GSH, was measured by Elisa kit and the data of the GOx@FeNPs+L group was consistent with ROS and LPO expression levels (Fig. 2E). GSSG concentration increased after laser irradiation due to the depletion of GSH, suggesting that combined PTT can accelerate cellular ferroptosis. The down-regulated of GPX4 protein is a typical indicator of ferroptosis, whose activation directly affects the intracellular GSH level. Therefore, the GPX4 expression level was analyzed by western blotting (Fig. 2F). Compared to other groups, the GPX4 level was remarkably down-regulated in GOx@FeNPs and GOx@FeNPs+L groups. Similarly, the decline was restored after the Fer-1 addition.

Quantitative analysis also revealed that the level of GPX4 in the control was 2.13-fold higher than that in the GOx@FeNPs+L group. Given all the above, the prepared nanoplateform successfully induced ferroptosis in CT26 cells. With the presence of GOx, it could significantly accelerate the Fenton reaction and subsequent ferroptosis. Moreover, when combined with PTT, the therapeutic efficiency could be further improved.

ICD induction and DC maturation by GOx@FeNPs in vitro

The research found that cancer cells undergoing ferroptosis will release DAMPs, including CRT, HMGB1, and ATP, which stimulate the maturation of DCs, and then activate the immune response [38]. And our previous findings demonstrated that PTT could also induce ICD in tumor cells. Thus, whether GOx@FeNPs could induce and improve ICD was investigated. As shown in Fig. 4A, there was a visible green fluorescence in the FeNPs and GOx@FeNPs groups without laser, indicating that Fe^{3+} induced ferroptosis and up-regulate CRT level. Meanwhile, the stronger fluorescence in GOx@FeNPs groups proved greater enzymatic activity of GOx, which enhanced the cellular ferroptosis effect. At the same time, the GOx@FeNPs+L group presented the strongest CRT signal, the highest extracellular HMGB1 concentration and the lowest intracellular ATP level (Fig. 4B and C), demonstrating that PTT combined with ferroptosis could significantly enhanced ICD of CT26 cells. To further investigate whether GOx@FeNPs-mediated PTT could activate the maturation of DCs, marrow-derived DCs isolated from mouse bone marrow were chosen to co-culture with CT26 cells with different formulations (Fig. 4D). After 24 h of stimulation, flow cytometry detected surface markers of mature DCs, including CD11c, CD80, and CD86. As illustrated in Fig. 4E and Figure S4, the FeNPs (67.2±0.16%) and GOx@FeNPs (68.2±1.59%) groups induced a much higher DCs maturation than that of the control (43.3±1.08%) even without laser due to the significant ferroptosis. Upon laser irradiation, the FeNPs+L and GOx@FeNPs+L groups comparatively increased to 73.8±4.99% and 82.1±1.48%, respectively, compared to 68.6% for DCs maturation in the reported work [30]. These findings revealed that GOx@FeNPs could activate a robust immune response featured by DCs maturation in vitro through PTT combined with ferroptosis, showing a improved ICD of cancer cells.

Magnetic properties and photothermal imaging of GOx@FeNPs

Given the presence of Fe^{3+} in GOx@FeNPs, the magnetic properties of GOx@FeNPs and its potential to be used as a contrast agent for guiding in vivo was investigated. The vibration sample magnetometer (VSM) test showed

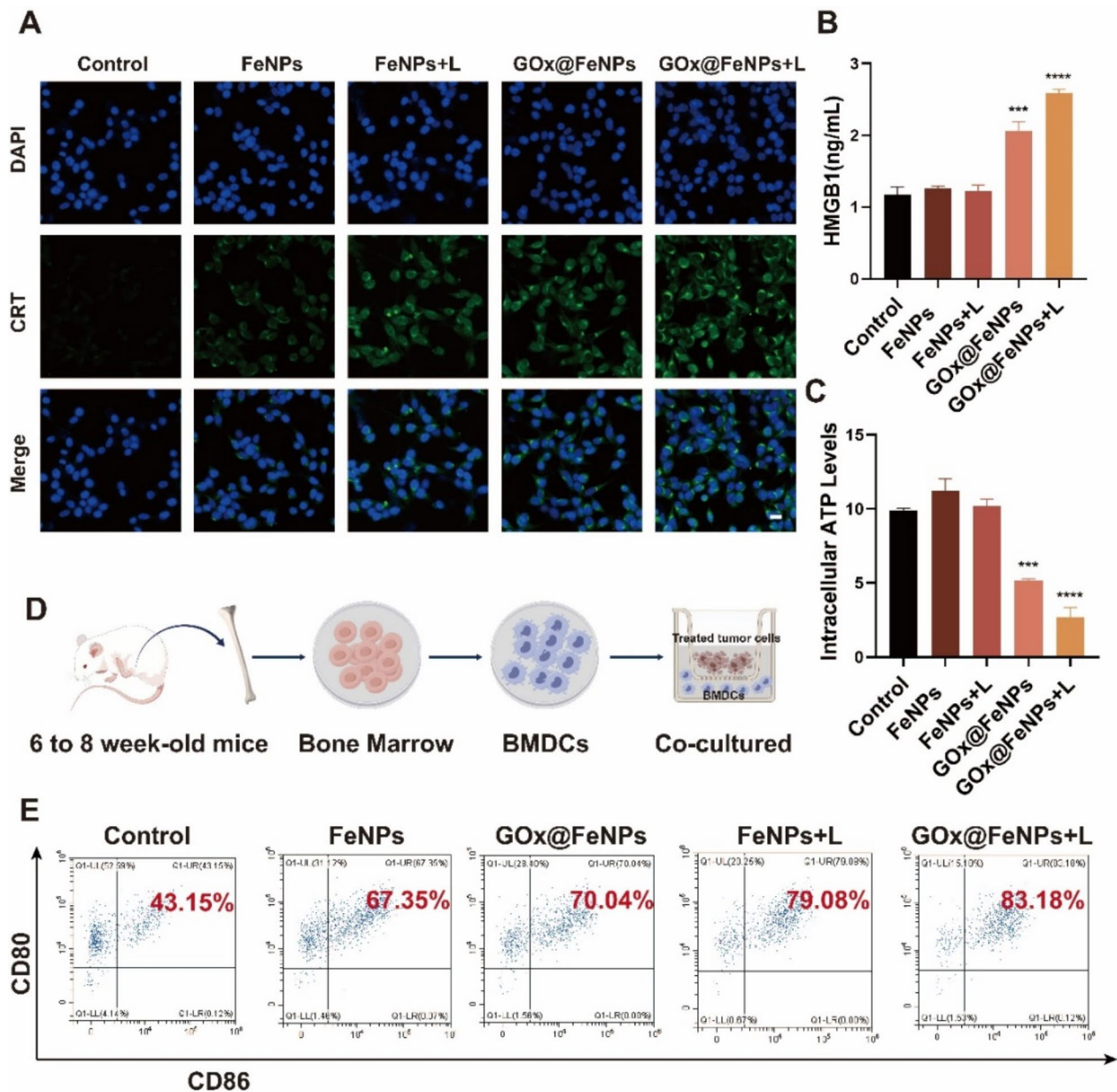


Fig. 4 ICD induction and DC maturation by GOx@FeNPs in vitro. **(A)** CLSM images of CRT in CT26 cells after FeNPs, FeNPs+L, GOx@FeNPs, GOx@FeNPs+L treated, green and blue fluorescence represent CRT and DAPI, respectively. (scale bar = 50 μ m). **(B)** Extracellular HMGB1 and **(C)** intracellular ATP release levels of CT26 cells following different formulation treatments as detected by Elisa kits (mean \pm SD; $n = 3$). **(D)** Transwell co-incubation experiment illustration. BMDCs were cultured in the lower chamber, and pretreated CT26 cells were in the upper. **(E)** Flow cytometry analysis of BMDCs maturation after different treatments. *** $p < 0.001$, **** $p < 0.0001$

that GOx@FeNPs had good superparamagnetic properties with a saturation magnetization strength of 47.22 emu/g (Fig. 5A). And apparent aggregation could be observed when the magnet was kept around the GOx@FeNPs solution (Fig. 5B), while the samples would be dispersed uniformly again without magnet, which demonstrated the excellent dispersion and magnetic responsiveness. Further, the magnetic resonance potential of GOx@FeNPs in vitro and in vivo was both explored. As shown in Fig. 5C, the T2 weighted signal was gradually

darkened with increasing concentrations of GOx@FeNPs, indicating a concentration-dependent behavior. Moreover, GOx@FeNPs were injected via tail vein into the CT26 tumor model of mice, which showed a gradually enhanced T2 weighted signal at the tumor site over time. The above results explained that GOx@FeNPs with dual targets possessed excellent tumor-targeted abilities. Additionally, it proved the potential use of GOx@FeNPs as contrast agents for tumor tracing therapy.

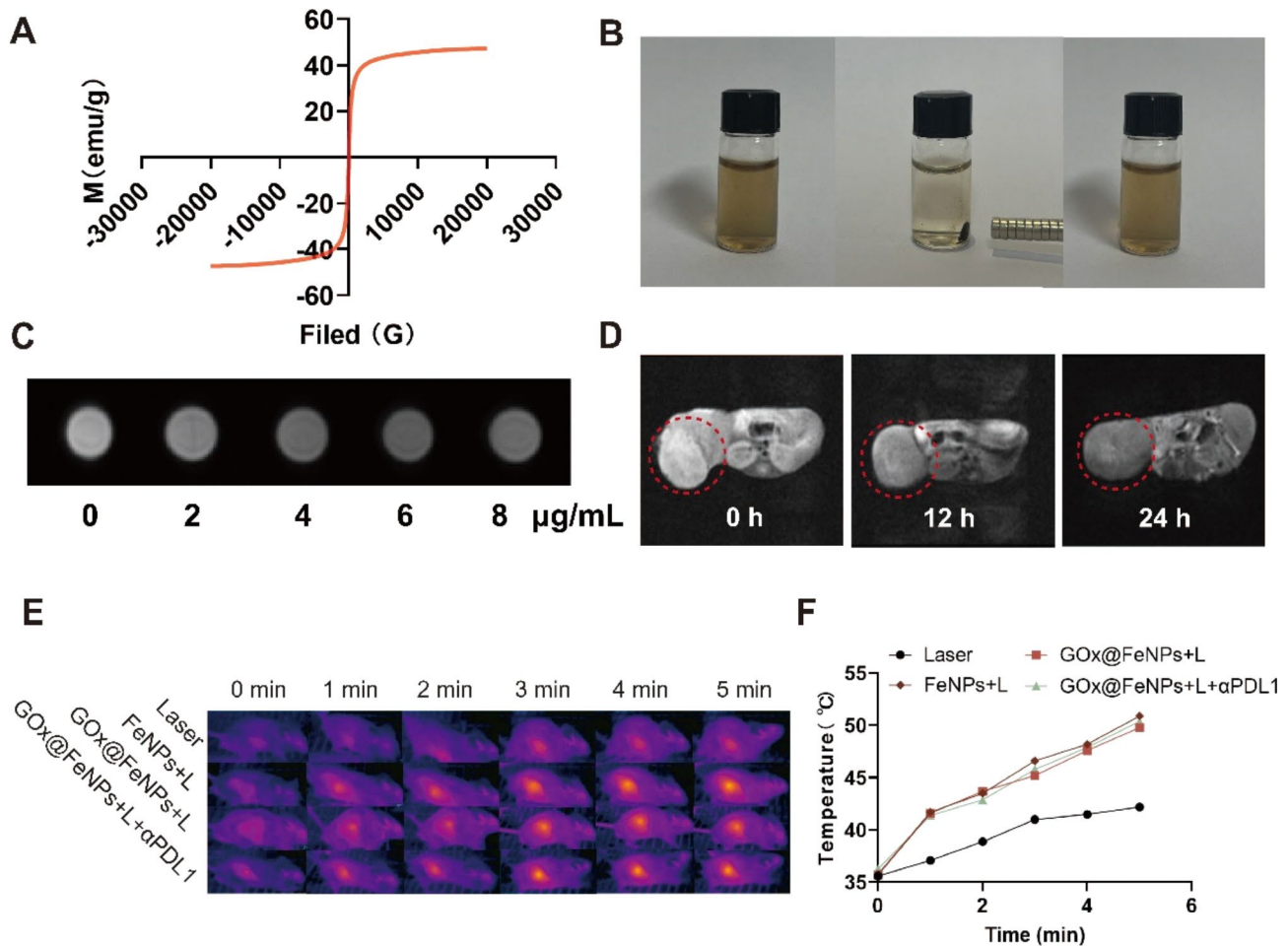


Fig. 5 Magnetic properties and photothermal imaging of GOx@FeNPs. **(A)** The magnetic hysteresis curves of GOx@FeNPs determined using VSM. **(B)** The magnet adsorption process of GOx@FeNPs suspensions in vitro. **(C)** T2 weighted MRI images of GOx@FeNPs suspension. **(D)** The T2 weighted MRI images at 0, 12, 24 h of CT26 tumor bearing mice after tail vein injection of GOx@FeNPs in vivo. Red dashed circles indicate tumors. **(E)** The thermal images of tumor bearing mice injected with different nano-formulations by tail vein under constant irradiation for 5 min. **(F)** Plot of temperature variation at tumor site, $n=6$

To evaluate the photothermal performance of nanoparticles in tumor bearing mice, FeNPs and GOx@FeNPs were injected by tail vein. When exposed to 808 nm irradiation ($1 \text{ W}/\text{cm}^2$), the treatment groups showed a rapid increase in temperature, reaching up to 49°C within 5 min in comparison to the control group (Fig. 5E and F). These results reconfirmed that GOx@FeNPs have favorable targeting, photothermal imaging, and photothermal ablation capabilities in vivo.

Anti-tumor performance of GOx@FeNPs in vivo

Based on the successful induction of ICD and activation of the immune response in vitro by GOx@FeNPs, the in vivo anti-tumor effects were examined combining with $\alpha\text{PD-L1}$ via Balb/c mice subcutaneous CRC models. In the treatment procedure Figs. 1 and 6A* 10^6 CT26-luc cells were inoculated subcutaneously in the right flank of Balb/c mice to establish a CRC model. Once the initial

tumor volume reached about 50 mm^3 , tumor-bearing mice were randomly divided into 8 groups and then treated 3 times with different nano formulations over 14 days. The formulations included the control, GOx, Laser, $\alpha\text{PD-L1}$, FeNPs+L, GOx@FeNPs, GOx@FeNPs+L, GOx@FeNPs+ $\alpha\text{PD-L1}$ +L. The body weight and tumor volume of mice in each group were monitored every 2 days after treatment. The Fig. 6B showed that there was no obvious body weight loss in all mice. And H&E staining of major organs (heart, liver, spleen, lungs, and kidneys) also demonstrated that the treated group had no significant pathologic toxicity (Figure S5). Furthermore, the liver and kidney function were performed on mice after co-treatment, including blood urea nitrogen (BUN), aspartate aminotransferase (AST), serum creatinine (CRE) and alanine aminotransferase (ALT). All physiologic indices were in the normal range compared with the PBS group, indicating the biosafety of GOx@

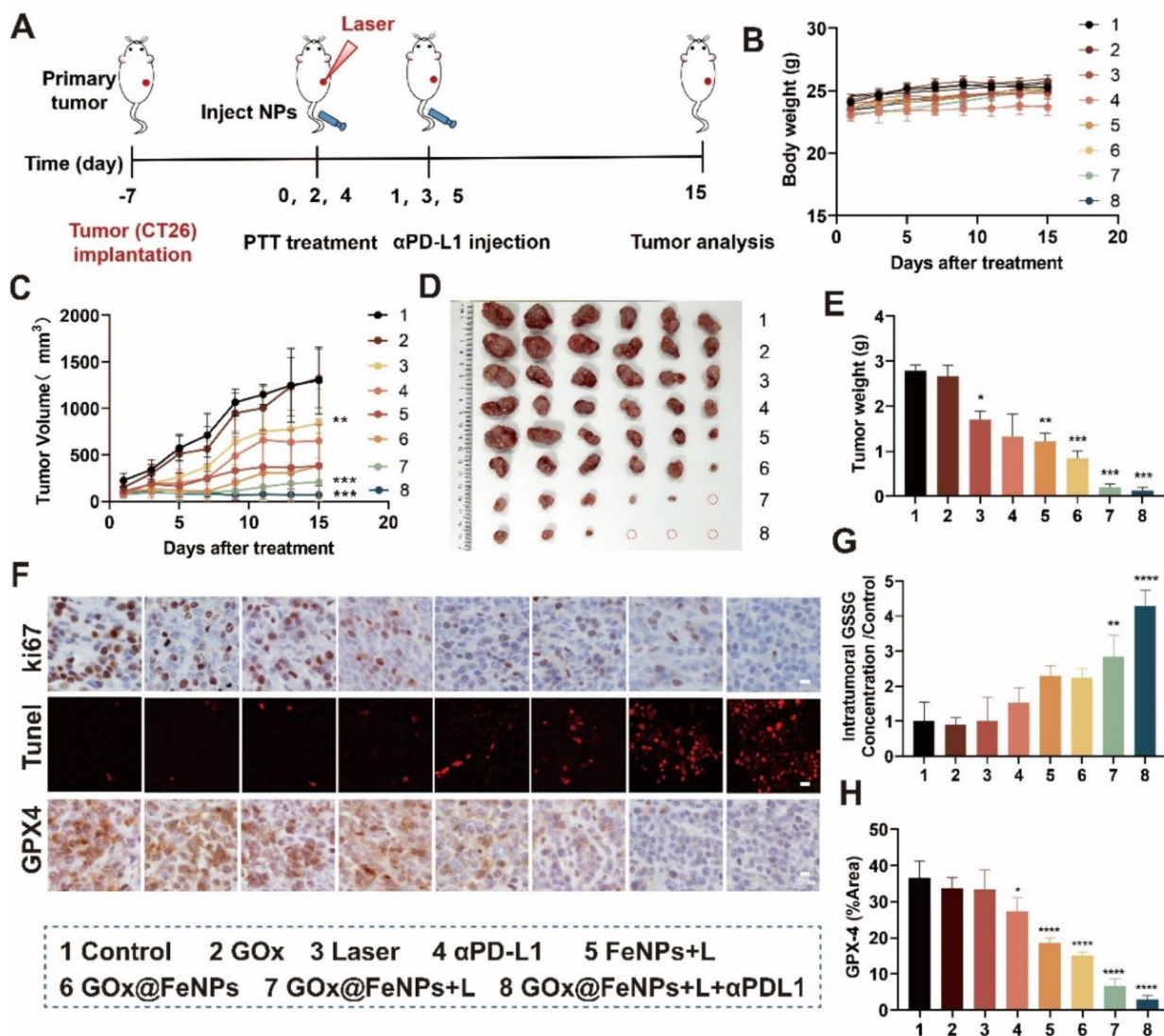


Fig. 6 Anti-tumor performance of GOx@FeNPs in vivo **(A)** Schematic illustration of tumor therapeutic protocols. **(B–C)** The body weight and tumor growth inhibition of mice after treatment in different groups. ($n=6$). **(D–E)** The tumor photographs and weights after different administrations. ($n=6$). **(F)** Representative Ki67, TUNEL, and GPX4 staining images of tumor tissue slices in different groups. Scale bar 10 μm . **(G)** The GSSG concentration in various groups of tumor tissues by Elisa assay (mean \pm SD; $n=3$). **(H)** The quantitative analysis of GPX4 immunohistochemistry in **(F)**. (mean \pm SD; $n=3$). * $p < 0.05$, ** $p < 0.01$, *** $p < 0.001$, **** $p < 0.0001$

FeNPs at the experimental dose (Figure S6). As compared with the control, tumor inhibition effectiveness in the GOx group was limited. It could be understood that the poor targeting properties made it readily cleared by the blood circulatory system. In the groups with $\alpha\text{PD-L1}$, the $\alpha\text{PD-L1}$ immune checkpoint blocker would bind to PD-L1, which blocked the PD-1/PD-L1 pathway, mediating tumor immune escape and enhancing CTLs activity. However, the therapeutic effect was unsatisfactory with $\alpha\text{PD-L1}$ alone due to the lower immunologic response (Fig. 6C). The stronger antitumor effects in the FeNPs+L and GOx@FeNPs groups was attributed to the FeNPs-mediated PTT synergizing with ferroptosis, which was

accelerated by the presence of the GOx enzyme. Hence, the GOx@FeNPs+L group, in sharp contrast, exhibited the strongest tumor inhibition effect, with a tumor suppression rate of 88.95%. Meanwhile, the inhibition was further enhanced by 91.13% combined with $\alpha\text{PD-L1}$, which was attributed to the fact that $\alpha\text{PD-L1}$ could sensitize the immunogenicity caused by ferroptosis and PTT. These results indicated that the co-administration of ICB achieved a synergistic and beneficial antitumor effect (Fig. 6C). The images and weight of the tumor in each group also followed the same trend as the volume (Fig. 6D and E). Next, tumor tissues were collected for the following TUNEL and Ki67 analysis. The strongest tumor

proliferation inhibition and the most significant tumor apoptosis were observed in the GOx@FeNPs+L+ α PD-L1, which reconfirmed the remarkable anti-tumor efficacy of it (Fig. 6F). The study also evaluated the ferroptosis efficacy in vivo, and the quantitative analysis showed that GPX4 expression was down-regulated significantly in the GOx@FeNPs+L and GOx@FeNPs+ α PD-L1+L groups (Fig. 6F and H). In addition, the concentration of intracellular GSSG gradually increased, indicating an increase in GSSG which meant the consumption of GSH. The above characteristic ferroptosis indicators also supported the tumor growth might be further suppressed by the GOx@FeNPs-mediated PTT and ferroptosis in a sensitive immune environment.

Immune response induced by GOx@FeNPs in vivo

As previously mentioned, GOx@FeNPs could activate antitumor immune responses through PTT and ferroptosis. Then apoptotic tumor fragments could stimulate the maturation of DCs so as to induce effective CD8⁺ T cell activation and infiltration, ultimately leading to an effective systemic immune response. To evaluate the underlying antitumor immune mechanism, lymph nodes, spleen, and tumor tissues from each group were collected for flow cytometry analysis, and the cytokines in serum were detected using an Elisa kit. As displayed in Fig. 7A and B, the maturation of DCs in lymph nodes was relatively low in the control ($4.56 \pm 1.18\%$), GOx ($8.66 \pm 3.67\%$), Laser ($8.51 \pm 1.06\%$), and α PD-L1 ($10.2 \pm 1.67\%$) groups. However, the GOx@FeNPs+L group showed a $19.3 \pm 3.80\%$ maturation of DCs, which was 4.60 times higher than that of the control. The maturation was further facilitated by using the α PD-L1, which was 1.31 times higher than that of GOx@FeNPs+L. The spleen is an essential tissue where lymphocytes are stimulated by antigens and immune response begins. As in Fig. 7C, D and E, the number of activated CD4⁺ and CD8⁺ T cells in the spleen of the GOx@FeNPs+L group was 2.38 and 2.13 times higher than that of the control respectively. Moreover, the GOx@FeNPs+L+ α PD-L1 group showed a further increase with 1.56 and 1.25 times more CD4⁺ and CD8⁺ T cells than the GOx@FeNPs+L group. These results reveal that GOx@FeNPs-mediated PTT and ferroptosis combined with ICB could effectively boost not only the maturation of DCs, but also the activation of CD4⁺ T cells and CTLs. Besides, immunofluorescence analysis further proved the infiltration of CD4⁺ and CD8⁺ T cells in the co-treatment group (Fig. 7F). The cytokines levels of interferon-gamma (IFN- γ), tumor necrosis factor-alpha (TNF- α), and interleukin 6 (IL-6) were also remarkably up-regulated in GOx@FeNPs+L+ α PD-L1, demonstrating that GOx@FeNPs-mediated PTT, ferroptosis combined with the α PD-L1 triggered a powerful anti-tumor immune response (Figure S7).

Conclusions

In conclusion, we developed co-therapeutic GOx@FeNPs nanoplatfoms that induced ICD via PTT and ferroptosis to ablate solid tumors by activating systemic anti-tumor immune responses. The nanoplatfoms have excellent targeting ability, and photothermal conversion characteristics, and can also act as potential contrast agents. Upon cellular uptake, GOx@FeNPs converted light energy into heat under laser irradiation, inducing ICD and tumor cell apoptosis. Additionally, GOx catalyzed glucose to H₂O₂, which reacted with the excess Fe³⁺ to generate \bullet OH synergistically increasing cytotoxic ROS. Thereby, leading to cellular ferroptosis and further enhancing ICD. After treatment with the nanoplatfoms, a large number of specific antigens were released, which promoted the maturation and antigen presentation of DCs. This induced the activation and proliferation of T cells, thus activating the systemic anti-tumor immunity to inhibit the growth of the tumor. Together with the α PD-L1, the therapeutic effect and associated anti-tumor immune response were significantly improved. We thus propose a promising combined therapeutic strategy for treating CRC by developing simple and multifunctional nanoplatfoms.

Experimental section

Materials

Magnetite (Fe₃O₄) was procured from Macklin (USA). Glucose oxidase (GOx) and dopamine hydrochloride (DA-HCl) were obtained from Sigma (USA) and Adamus Reagent GmbH (Switzerland), respectively. Bifunctional PEG (NH₂-PEG-MAL) with amino and maleimide groups was sourced from Yangtuo Biotechnology (Shanghai). The live/dead cell double staining kit was acquired from the Tongren Institute of Chemistry. For detecting adenosine triphosphate (ATP) and reactive oxygen species (ROS), assay kits were purchased from Beyotime Biotechnology (Shanghai). Additionally, the glutathione disulfide (GSSG) assay kit was supplied by Beijing Box Biotechnology. BODIPY^{581/591}-C11 was purchased from Thermo Fisher (Waltham, MA). Antibodies against CRT, GPX4, Ki67, CD4, CD8, and fluorescently labeled secondary antibodies were purchased from Abcam (UK). Antibodies against CD11c and CD80, as well as CD86, were obtained from Biolegend (USA) and Invitrogen (USA), respectively. Anti- β -actin was purchased from Cell Signaling Technology (USA). The terminal deoxynucleotidyl transferase dUTP nick end labeling (TUNEL) assay kit was purchased from Roche (Switzerland). The IFN- γ detection kit was purchased from Biodragon Biotechnology (Beijing), the IL-6 detection kit was obtained from Wuhan Huamei Biotechnology, and the TNF- α detection kit was sourced from Wuhan Xinbosheng Biotechnology.

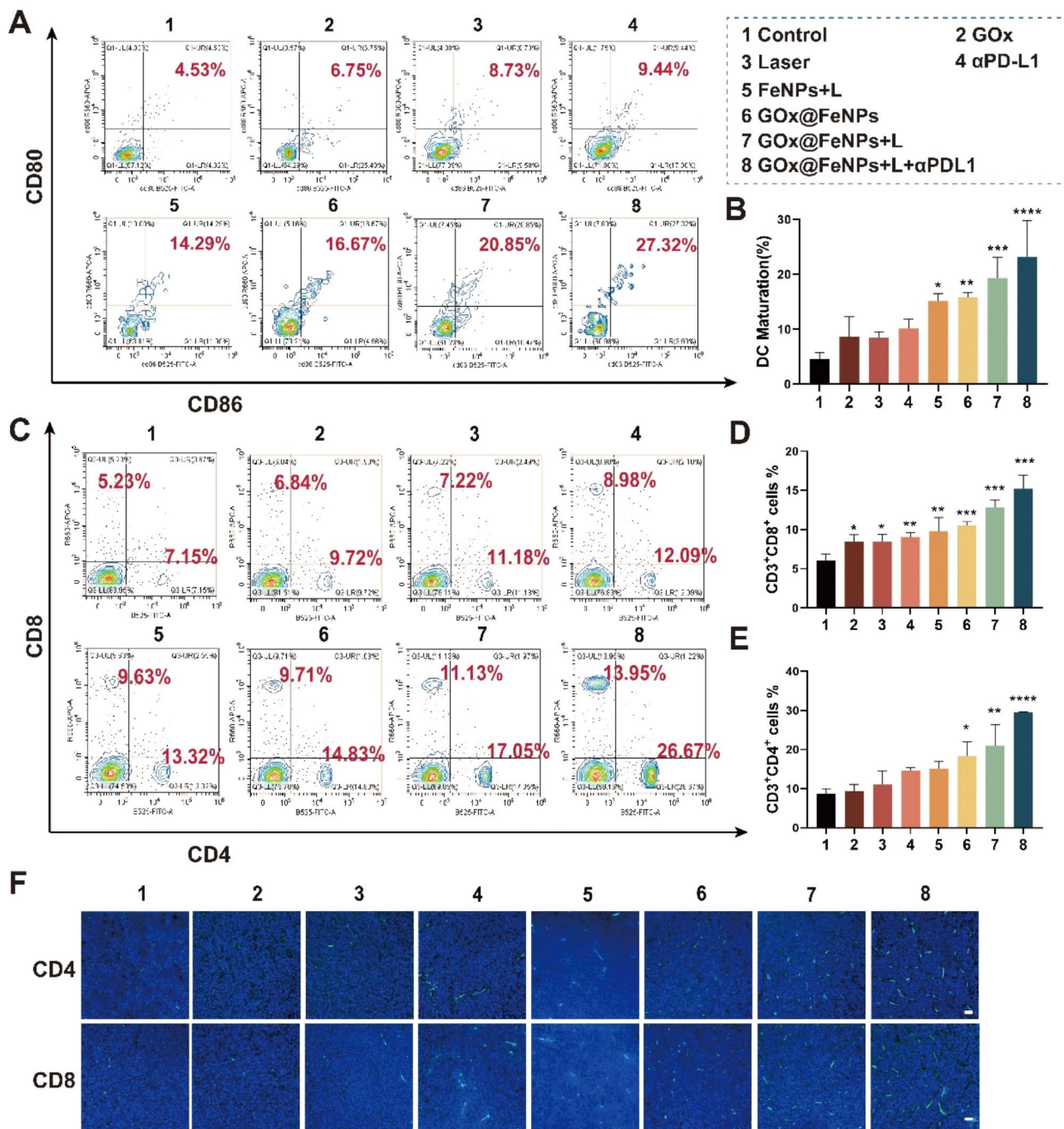


Fig. 7 Immune response induced by GOx@FeNPs in vivo. **(A)** Flow cytometry analysis of CD11c⁺ CD80⁺ CD86⁺ in lymph nodes of various groups in mice. **(B)** Quantitative analysis of DCs maturation (mean ± SD; n = 3). **(C)** Flow cytometry analysis of CD3⁺ CD4⁺ and CD3⁺ CD8⁺ T cells in spleens after various treatments in mice. **(D-E)** Quantitative analysis of CD4⁺, CD8⁺ T cells in spleens (mean ± SD; n = 3). **(F)** Immunofluorescence analysis of CD4⁺, CD8⁺ T cells in tumor tissue slices of mice in various groups. Scale bar = 50 μm. *p < 0.05, **p < 0.01, ***p < 0.001, ****p < 0.0001

Cell lines and animals

The CT26 mouse CRC cell line was obtained from the Institute of Biochemistry and Cell Biology, Chinese Academy of Sciences in Shanghai, China. The cells were grown in RPMI-1640 complete medium with 10% fetal bovine serum and 1% streptomycin-penicillin, and were cultured in a humidified environment with 5% CO₂ at 37

°C. When the cells reached 80% confluence, they were detached using 0.25% trypsin/EDTA solution.

Balb/c mice (6–8 weeks old, weighing (20.0 ± 0.5) g) were purchased from Bikai Keyi Biotechnology in Shanghai, China. All animal experiments were conducted in accordance with the regulations of the Ethics Committee

of Putuo Hospital, Shanghai University of Traditional Chinese Medicine, China.

Synthesis and characterization of the GOx@FeNPs

The preparation of GOx@FeNPs was based on our previous work and optimized the process [53]. Firstly, 10 mg of Fe₃O₄ nanoparticles were added into 10 mL of Tris buffer containing 5 mg of dopamine hydrochloride. The mixture was stirred at 300 rpm for 3 h at room temperature to obtain Fe₃O₄@PDA. Next, the pre-prepared NH₂-PEG-cRGD as well as NH₂-PEG-AA solutions were added dropwise under stirring at room temperature and left to react overnight. The unattached target was then removed by centrifugation, yielding Fe₃O₄@PDA-PEG-cRGD-AA NPs (FeNPs). The above FeNPs were weighed and dissolved in deionized water, to which GOx aqueous solution (100 µg/mL) was added dropwise. After ultrasonic dispersion for 5 min, it was reacted on a shaking bed for 12 h, and the precipitate was washed several times with deionized water to obtain GOx@FeNPs. The morphology of the GOx@FeNPs was observed using transmission electron microscopy (TEM, JEOL Ltd., Tokyo, Japan), and the particle size and the zeta potential were determined by Malvern Zetasizer Nano Z (Malvern, UK).

In vitro photothermal performance

To evaluate the photothermal conversion performance of GOx@FeNPs in vitro, different concentrations of GOx@FeNPs (0, 25, 50, and 100 µg/mL) were exposed to 808 nm NIR at a power density of 1.0 W/cm² (MDL-F-808, Changchun New Industries Optoelectronics Technology Co., Ltd). The temperature change was monitored and recorded using a NIR thermal camera.

To investigate the photothermal stability of GOx@FeNPs in vitro, a 100 µg/mL solution of GOx@FeNPs was exposed to 808 nm NIR laser for 5 min repeatedly. After each cycle, the solution was allowed to cool to room temperature naturally, and the temperature was recorded every minute for a total of 5 cycles.

Magnetic capacity and MRI

To determine the magnetic properties of the prepared nanomaterials in vitro, 10 mg of GOx@FeNPs powder was used to characterize its hysteresis properties with the help of a vibrating sample magnetometer (LakeShore, USA) at room temperature. Additionally, a suspension of GOx@FeNPs at a concentration of 100 µg/mL was prepared and transferred to a syringe bottle to observe its dispersion in water. A magnet was placed on one side of the bottle for 1 min, and after removing it, a period was waited for observation and recording.

To assess the in vitro MRI performance, GOx@FeNPs solutions at different concentrations (0, 2, 4, 6 and 8 µg/

mL) were added to 1.5 mL Eppendorf tubes, mixed and then imaged using a T2 MRI scanner.

To evaluate the in vivo MRI, Balb/c tumor-bearing mice with a tumor volume of approximately 500 mm³ were selected. After intravenous injection of 200 µL of GOx@FeNPs (2 mg/mL), T2-weighted MRI of the anesthetized mice was performed at 0, 12, and 24 h intervals. The MRI parameters were set as follows: TR=2500 ms, TE=90 ms, FOV=100 mm, and slice thickness=3 mm.

Cellular uptake

The CT26 cells were cultured uniformly in confocal dishes with approximately 3.5×10⁵ cells per well in the control group. GOx@FeNPs (100 µg/mL) labeled with 1.0 µg/mL coumarin 6 (Ce6) were added to replace the original medium, and different incubation times were set at 0, 2, 4, and 6 h. Furthermore, to demonstrate the targeting ability, RGD and AA were added and pre-treated for 0.5 h before replacing with GOx@FeNPs/Ce6 medium, where incubation was continued for 4 h. At the end of incubation, cells from all groups were washed with PBS for 5 min, fixed with paraformaldehyde and stained with DAPI. After 5 min incubation at room temperature, fluorescence intensity was observed using a CLSM (Carl Zeiss Germany).

Cytotoxicity assay

The CT26 cells were seeded into a 96 well plate at a density of 1×10⁴ cells per well and maintained in 100 µL RPMI 1640 complete medium. After 24 h, the old medium was replaced with 100 µL of fresh medium, which contained different concentrations of Fe₃O₄@PDA, ranging from 0 to 200 µg/mL. Additionally, a fresh medium containing different nanomaterials at a Fe concentration of 100 µg/mL was also used, including control, Fe₃O₄@PDA, FeNPs, and GOx@FeNPs. The cells were then exposed to 808 nm laser (1 W/cm²) for 5 min after 4 h, followed by replacement with complete culture medium and further incubation for 24 h. The relative cell viability of each group was evaluated using the CCK-8 assay (Dojindo). Additionally, PI (dead cells, red) and Calcein-AM (live cells, green) staining were also performed, and fluorescence images were captured using an inverted fluorescence microscope (Leica).

ICD

To detect the extracellular HMGB1 concentration and intracellular ATP level, 1.5×10⁵ CT26 cells were cultured in 500 µL of complete medium in 24 well plates. After 24 h, the cells were treated with different nanoparticles, control, FeNPs, FeNPs+L, GOx@FeNPs, GOx@FeNPs+L in 500 µL of fresh medium. After 4 h, the cells were rinsed with PBS and irradiated with an 808 nm laser (1 W/cm²) for 5 min, then replaced with complete

medium and continued to culture for another 24 h. The supernatant was collected to measure mouse HMGB1 using an ELISA kit (ELISA), and cells were harvested for ATP analysis following the manufacturer's instructions.

To detect CRT exposure, CT26 cells were seeded at a density of 3.5×10^5 in confocal dishes and cultured for 24 h using the same treatments as described in the HMGB1 experiment. After 24 h of incubation, cells were immobilized with 4% paraformaldehyde for 5 min, permeabilized with 0.1% Triton X-100 for 5 min, and then rinsed three times with PBS. It was then blocked with 5% fetal bovine serum for 1 h and stained with Alexa Fluor 488-CRT antibody (ab196158) at 4 °C overnight. Then the cells were rinsed with PBS and stained with DAPI for 5 min. Finally, a CLSM was used for imaging.

DC maturation in vitro

In this study, Balb/c mice (3–5 weeks old, male) were used. The mice were humanely euthanized using the cervical dislocation method, and the hind legs were skinned to carefully extract the bilateral femurs and tibiae. The bone marrow was then harvested by inserting a needle and suctioning repeatedly until the cavity turns white. The cells were then resuspended in a medium containing 10% FBS, 10 ng/mL GM-CSF, and 1 ng/mL IL-4 in RPMI-1640. The cell concentration was adjusted to 2×10^6 and placed in transwell chambers, which were cultured for 72 h. Following this, CT26 cells that had been treated with different nanoformulations were added to the upper chamber and co-cultured for an additional 24 h after 4 h of NIR irradiation. The DCs from different groups were collected, blocked with 2% Fc block for 5 min, and incubated with antibodies CD11c (Biolegend), CD80 (Biolegend) and CD86 (Invitrogen) 30 min and then detected by flow cytometry.

Intracellular ROS generation

The CT26 cells were cultured in confocal dishes at a density of 3.5×10^5 cells per dish. After 24 h of incubation, the cells were treated with different preparations of nanoparticles, including control, GOx@FeNPs, GOx@FeNPs+L, and the ferroptosis inhibitor ferrostatin-1 (Fer-1). Following 4 h of co-culture, the laser group was irradiated with 808 nm (1 W/cm^2) and the cells were further incubated for 24 h. An additional 10 μM DCFH-DA solution was added to the cells and incubated at 37 °C for another 20 min. The cells were washed several times with PBS and the fluorescence was observed by CLSM.

Intracellular LPO generation

The CT26 cells were cultured overnight in confocal dishes at a density of 3.5×10^5 cells per dish. When the cells grew to 80%, the experimental settings were control, GOx@FeNPs, GOx@FeNPs+L, and GOx@

FeNPs+L+Fer-1 (equivalent Fe concentration ($100 \mu\text{g mL}^{-1}$)). After 4 h of incubation, the cells were exposed to an 808 nm laser for 5 min and then allowed to incubate for another 24 h. Afterward, the medium was discarded and replaced with a serum-free 1640 medium containing BODIPY^{581/591}-C11 at a concentration of 1 μM , which was incubated with the cells for 30 min at 37 °C for CLSM observation.

Intracellular GPX4 expression level

The western blotting assay was conducted to analyze the intracellular expression levels of GPX4. Briefly, CT26 cells were seeded in 24 well plates at a density of 1.5×10^5 cells per well and incubated overnight. When the cell density reached 80%, the experiments were performed with the equivalent Fe concentration ($100 \mu\text{g mL}^{-1}$) of the corresponding drugs. After 4 h of incubation, the laser group was irradiated at 808 nm (1 W/cm^2) and then incubated for an additional 24 h. The cells were washed three times with PBS, and total cellular protein was prepared in lysis buffer and quantified using a Bradford kit. A total of 20 μg of protein samples were separated by 15% SDS-PAGE and then transferred to polyvinylidene difluoride (PVDF) membranes. Next, protein blots were incubated with rabbit GPX4 (Abcam) primary antibody (1:1000) at 4 °C overnight, followed by horseradish peroxidase-conjugated secondary antibody (1:10000) at 37 °C for 1 h. Rabbit β -actin (1:1000) was used as a protein loading control. The specific protein bands were imaged using enhanced chemiluminescence (ECL).

Intracellular GSSG level

The expression of GSSG in cells was measured under various treatments using ELISA kits according to standard protocols.

In vivo photothermal thermal image

To evaluate the photothermal effect of GOx@FeNPs in vivo, it was administered via injection through the tail vein of tumor-bearing mice. After 24 h, the tumor area was irradiated with an 808 nm (1 W/cm^2) laser for 5 min duration. Temperature changes were monitored and recorded throughout the process using an NIR thermal camera.

In vivo antitumor effect

To establish a tumor-bearing mouse model, 1×10^6 of luciferase-labeled CT26 cells were injected subcutaneously into the right side of 6–8-week-old Balb/c female mice. When the tumor volume reached 50 mm^3 , the mice were randomly divided into 8 groups ($n=6$): (1) Control, (2) GOx, (3) Laser, (4) $\alpha\text{PD-L1}$, (5) FeNPs+L, (6) GOx@FeNPs, (7) GOx@FeNPs+L, (8) GOx@FeNPs+L+ $\alpha\text{PD-L1}$. Subsequently, different nano-preparations were

injected via the tail vein at days 0, 2, and 4. In the laser group, the tumor site was irradiated with 808 nm NIR laser at a power of 1.0 W/cm² for 5 min after 24 h of administration. It was also monitored and recorded by NIR thermal camera until it reached about 48 °C. While all α PDL1 group was injected intravenously on days 1, 3 and 5, respectively. Tumor volumes and the body weight of mice were recorded every two days from the beginning of treatment. The formula for calculating tumor volume was: volume = (long diameter \times short diameter \times short diameter)/2.

To investigate the combined therapy effect, all mice were executed when the tumors reached about 2000 mm³. The serum, tumors, and essential organs such as the heart, liver, spleen, lungs, kidneys, and lymph nodes were also collected. The spleen and lymph nodes were used to detect immune cells, while the other tissues were fixed in paraformaldehyde for 48 h for further analysis.

In vivo antitumor immune response

Freshly isolated lymph nodes and spleens were cut, ground, and filtered through a 70 μ m cell filter to prepare cell suspensions. For spleen cells, an additional amount of erythrocyte lysate was required. Afterward, the cells were incubated with Fc-Block (biogend) to avoid non-specific binding. To analyze mature DCs in lymph nodes, CD11c-Cy5.5 (biogend), CD80-APC (biogend), and CD86-FITC (Invitrogen) staining were used. Additionally, staining with CD3-PE (Abcam), CD4-FITC (Abcam), and CD8a-APC (Abcam) were performed to analyze helper T cells (Ths, CD3⁺CD4⁺) and CTLs, CD3⁺CD8⁺). After washing, the cells were resuspended in stain buffer and then analyzed using flow cytometry (Beckman, USA).

Immunohistochemistry assays

The collected tumor tissues of each group were carefully sliced and processed for antigen retrieval using 1 \times sodium citrate. Then, dropwise added 3% H₂O₂ solution, followed by blocking with 5% BSA. The slices were then stained with Ki67 (Abcam) and GPX4 (Abcam) antibodies, rinsed three times with PBS, and incubated with secondary goat anti-rabbit immunoglobulin G (IgG) for 30 min at 37 °C. After rinsing with PBS, the slides were incubated with the chromogenic kit DAB. Finally, the slides were rinsed with water, stained with hematoxylin for 10 s, and sealed for microscopic observation.

Immunofluorescence assays

To assess immunofluorescence staining, the antigen repair and blocking processes were carried out as described in the immunohistochemical study. The tissues were then incubated with primary antibodies for CD4 (Abcam) and CD8 (Abcam) overnight at 4 °C, followed by a donkey anti-rabbit IgG for 1 h at room temperature.

Finally, it was stained with DAPI, sealed, observed and photographed under CLSM.

TUNEL

To evaluate apoptosis in the tumor tissues, the slices were stained using the TUNEL assay kit according to the instructions of the manufacturer. Fluorescence images were then captured using CLSM.

In vivo cytokine assay

In the study, serum samples were collected from each group and the levels of TNF- α (EMC102a), IFN- γ (BDEL-0054), and IL-6 (E04639m) were measured using ELISA kits as the instructions provided by the manufacturer.

Biosafety

The main organs, including heart, liver, spleen, lungs, and kidneys of the tumor-bearing mice were collected to evaluate the tissue integrity. It was fixed in 10% formalin, embedded in paraffin, and 4 μ m sections were prepared. The slices of each group were then stained with H&E and observed under a microscope (Leica). Besides, mouse serum levels of BUN, AST, CRE and ALT were purchased from Nanjing Jiancheng Bioengineering Institute, China, and the detailed methods were provided by the manufacturer.

Statistical analysis

One-way analysis of variance (ANOVA) or t test for multiple comparisons was used for statistical analysis. All data were expressed as mean \pm standard deviation (SD). Statistical significance was set at * p < 0.05, ** p < 0.01 and *** p < 0.001, **** p < 0.0001, as indicated in the figures.

Supplementary Information

The online version contains supplementary material available at <https://doi.org/10.1186/s12951-024-02909-3>.

Supplementary Material 1

Acknowledgements

We thank to the Figdraw for the drawing material. Meanwhile, we appreciate the supports from the Shanghai Postdoctoral Excellence Program (2023551) of Shanghai Municipal Human Resource and Social Security Bureau, as well as the Postdoctoral Fellowship Program (Grade C, GZC20231695) of China Postdoctoral Science Foundation.

Author contributions

PY, ZY and XY conceived, designed the experiments and revised the manuscript. YL and JC performed the experiments and wrote the manuscript. QX and JS collected the data and analysis. ZL revised the manuscript, YH and YC assisted in the animal experiments. FG assisted in the nanoparticles preparation. All authors reviewed the manuscript.

Funding

This work was financially supported by the National Natural Science Foundation of China (Grants Numbers: 81973700), Clinical Specialized Discipline of Health System of Putuo District in Shanghai (Grants Numbers: 2021tszk01), Shanghai University of Traditional Chinese Medicine Science

and Technology Development Project (Grants Numbers: 23KFL084) and Postdoctoral Research Project of Putuo Hospital affiliated to Shanghai University of Traditional Chinese Medicine (2023-BSH-01).

Data availability

All data are available in the main text, supporting information, and are also on request from the corresponding author.

Declarations

Ethics approval and consent to participate

All the mice used in the experiment were carefully bred at Putuo Hospital of Shanghai University of Traditional Chinese Medicine. The experiment followed the ethical norms and received the ethical approval number: DWEC-A-202308004.

Competing interests

The authors declare no competing interests.

Received: 7 June 2024 / Accepted: 5 October 2024

Published online: 16 October 2024

References

- Rastin F, Javid H, Oryani MA, Rezagholinejad N, Afshari AR, Karimi-Shahri M. Immunotherapy for colorectal cancer: rational strategies and novel therapeutic progress. *Int Immunopharmacol*. 2024;126:111055.
- Li J, Wu C, Hu H, Qin G, Wu X, Bai F, Zhang J, Cai Y, Huang Y, Wang C, et al. Remodeling of the immune and stromal cell compartment by PD-1 blockade in mismatch repair-deficient colorectal cancer. *Cancer Cell*. 2023;41:1152–e11691157.
- Fan A, Wang B, Wang X, Nie Y, Fan D, Zhao X, Lu Y. Immunotherapy in colorectal cancer: current achievements and future perspective. *Int J Biol Sci*. 2021;17:3837–49.
- Zhou Y, Li H, Zhang Y, Zhao E, Huang C, Pan X, Shu F, Liu Z, Tang N, Li F, Liao W. Deubiquitinase USP4 suppresses antitumor immunity by inhibiting IRF3 activation and tumor cell-intrinsic interferon response in colorectal cancer. *Cancer Lett*. 2024;589:216836.
- Takei S, Tanaka Y, Lin YT, Koyama S, Fukuoka S, Hara H, Nakamura Y, Kuboki Y, Kotani D, Kojima T, et al. Multiomic molecular characterization of the response to combination immunotherapy in MSS/pMMR metastatic colorectal cancer. *J Immunother Cancer*. 2024;12:e008210.
- Xi Y, Chen L, Tang J, Yu B, Shen W, Niu X. Amplifying eat me signal by immunogenic cell death for potentiating cancer immunotherapy. *Immunol Rev*. 2024;321:94–114.
- Ruan H, Leibowitz BJ, Zhang L, Yu J. Immunogenic cell death in colon cancer prevention and therapy. *Mol Carcinogen*. 2020;59:783–93.
- Limagne E, Thibaudin M, Nuttin L, Spill A, Derangère V, Fumet J-D, Amellal N, Peranzoni E, Cattani V, Ghiringhelli F. Trifluridine/Tipiracil plus Oxaliplatin improves PD-1 blockade in Colorectal Cancer by Inducing Immunogenic Cell Death and Depleting macrophages. *Cancer Immunol Res*. 2019;7:1958–69.
- Zeting Y, Shuli M, Yue L, Haowei F, Jing S, Yueping Z, Jie W, Teng C, Wanli D, Zhang K, Peihao Y. Tissue adhesive indocyanine green-locking granular gel-mediated photothermal therapy combined with checkpoint inhibitor for preventing postsurgical recurrence and metastasis of colorectal cancer. *Bioeng Transl Med*. 2023;8:e10576.
- Lu Y, Wang Y, Liu W, Ma H, Yang B, Shao K, Long S, Sun W, Du J, Fan J, et al. Photothermal nano-dot reactivate immune-hot for tumor treatment via reprogramming cancer cells metabolism. *Biomaterials*. 2023;296:122089.
- Li G, Zhang J, Zhang S, Teng L, Sun F. Multifunctional nanoadjuvant-driven microenvironment modulation for enhanced photothermal immunotherapy in breast cancer. *J Control Release*. 2023;362:309–24.
- Zhao X, Chen Y, Niu R, Tang Y, Chen Y, Su H, Yang Z, Jing X, Guan H, Gao R, Meng L. NIR Plasmonic nanozymes: synergistic enhancement mechanism and multi-modal Anti-infection applications of MXene/MOFs. *Adv Mater*. 2024;36:e2307839.
- Yongmei Wang HW, Yuhua Song M, Lv Y, Mao H, Song Y, Wang G, Nie X, Liu Jian Cui and Xueqing Zou: IR792-MCN@ZIF-8-PD-L1 siRNA drug delivery system enhances photothermal immunotherapy for triple-negative breast cancer under near-infrared laser irradiation. *J Nanobiotechnol*. 2022;20:96.
- Zhou B, Wu Q, Wang M, Hoover A, Wang X, Zhou F, Towner RA, Smith N, Saunders D, Song J, et al. Immunologically modified MnFe₂O₄ nanoparticles to synergize photothermal therapy and immunotherapy for cancer treatment. *Chem Eng J*. 2020;396:125239.
- Yu Y, Li J, Song B, Ma Z, Zhang Y, Sun H, Wei X, Bai Y, Lu X, Zhang P, Zhang X. Polymeric PD-L1 blockade nanoparticles for cancer photothermal-immunotherapy. *Biomaterials*. 2022;280:121312.
- Xu K, Wu X, Cheng Y, Yan J, Feng Y, Chen R, Zheng R, Li X, Song P, Wang Y, Zhang H. A biomimetic nanoenzyme for starvation therapy enhanced photothermal and chemodynamic tumor therapy. *Nanoscale*. 2020;12:23159–65.
- Xue C, Sutrisno L, Li M, Zhu W, Fei Y, Liu C, Wang X, Cai K, Hu Y, Luo Z. Implantable multifunctional black phosphorus nanoformulation-deposited biodegradable scaffold for combinational photothermal/ chemotherapy and wound healing. *Biomaterials*. 2021;269:120623.
- Zhao B, Hu X, Chen L, Wu X, Wang D, Wang H, Liang C. Fe₃O₄@TiO₂ microspheres: harnessing O₂ release and ROS Generation for Combination CDT/PDT/PTT/Chemotherapy in Tumours. *Nanomaterials*. 2024;14:498.
- Li R, Liu C, Wan C, Liu T, Zhang R, Du J, Wang X, Jiao X, Gao R, Li B. A targeted and pH-Responsive Nano-Graphene Oxide Nanoparticle loaded with doxorubicin for Synergetic Chemo-Photothermal therapy of oral squamous cell carcinoma. *Int J Nanomed*. 2023;18:3309–24.
- Zeng J, Yang L, Zeng L, Feng C, Yang Y, Ye Y, Zhang W, He J, Zhang C. Visualizing cancer resistance via nano-quenching and recovery detector of CD44. *J Nanobiotechnol*. 2024;22:452.
- Tang H, Chen J, Qi LH, Lyu M, Quan H, Tan ZJ. Multifunctional AuPt nanoparticles for synergistic Photothermal and Radiation Therapy. *Int J Nanomed*. 2023;18:6869–82.
- Yin M, Chen X, Guo Q, Xiao L, Gao P, Zang D, Dong J, Zha Z, Dai X, Wang X. Ultrasmall zirconium carbide nanodots for synergistic photothermal-radiotherapy of glioma. *Nanoscale*. 2022;14:14935–49.
- Ni J, Xu H, Zhong Y, Zhou Y, Hu S. Activatable UCL/CT/MR-enhanced in vivo imaging-guided radiotherapy and photothermal therapy. *J Mater Chem B*. 2022;10:549–61.
- Zhang C, Xia D, Liu J, Huo D, Jiang X, Hu Y. Bypassing the immunosuppression of myeloid-derived suppressor cells by reversing Tumor Hypoxia using a platelet-inspired platform. *Adv Funct Mater*. 2020;30:2000189.
- Li Q, Qin S, Tian H, Liu R, Qiao L, Liu S, Li B, Yang M, Shi J, Nice EC, et al. Nano-Econazole enhanced PD-L1 checkpoint blockade for synergistic Antitumor Immunotherapy against Pancreatic Ductal Adenocarcinoma. *Small*. 2023;19:e2207201.
- Cui M, Tang D, Wang B, Zhang H, Liang G, Xiao H. Bioorthogonal guided activation of cGAS-STING by AIE Photosensitizer nanoparticles for targeted tumor therapy and imaging. *Adv Mater*. 2023;35:e2305668.
- Zhang P, Wu Q, Yang J, Hou M, Zheng B, Xu J, Chai Y, Xiong L, Zhang C. Tumor microenvironment-responsive nanohybrid for hypoxia amelioration with photodynamic and near-infrared II photothermal combination therapy. *Acta Biomater*. 2022;146:450–64.
- Xu P, Liang F. Nanomaterial-based Tumor Photothermal Immunotherapy. *Int J Nanomed*. 2020;15:9159–80.
- Beniwal N, Verma A, Putta CL, Rengan AK. Recent trends in bio-nanomaterials and non-invasive combinatorial approaches of Photothermal Therapy against Cancer. *Nanotheranostics*. 2024;8:219–38.
- Chen M, Shen Y, Pu Y, Zhou B, Bing J, Ge M, Zhu Y, Gao S, Wu W, Zhou M, Shi J. Biomimetic inducer enabled dual ferroptosis of tumor and M2-type macrophages for enhanced tumor immunotherapy. *Biomaterials*. 2023;303:122386.
- Zeng L, Ding S, Cao Y, Li C, Zhao B, Ma Z, Zhou J, Hu Y, Zhang X, Yang Y, et al. A MOF-based potent ferroptosis inducer for enhanced Radiotherapy of Triple negative breast Cancer. *ACS Nano*. 2023;17:13195–210.
- Wang S, Guo Q, Xu R, Lin P, Deng G, Xia X. Combination of ferroptosis and pyroptosis dual induction by triptolide nano-MOFs for immunotherapy of Melanoma. *J Nanobiotechnol*. 2023;21:383.
- Zhou L, Chen J, Li R, Wei L, Xiong H, Wang C, Chai K, Chen M, Zhu Z, Yao T, et al. Metal-polyphenol-Network Coated Prussian Blue Nanoparticles for Synergistic Ferroptosis and apoptosis via triggered GPX4 inhibition and concurrent in situ Bleomycin Toxication. *Small*. 2021;17:e2103919.
- Li X, Lan Y, Fu X, Luo X, Chen J, Zhang W, Zuo B, Yang T, Liu B, Zhang C, Guo H. DNA nanomachine-driven chemodynamic therapy against glioblastoma. *Aggregate*. 2024:e603.
- Wang Y, Wu X, Bao X, Mou X. Progress in the mechanism of the Effect of Fe(3) O(4) nanomaterials on ferroptosis in Tumor cells. *Molecules*. 2023;28:4562.

36. Bayir H, Dixon SJ, Tyurina YY, Kellum JA, Kagan VE. Ferroptotic mechanisms and therapeutic targeting of iron metabolism and lipid peroxidation in the kidney. *Nat Rev Nephrol.* 2023;19:315–36.
37. Cui W, Guo M, Liu D, Xiao P, Yang C, Huang H, Liang C, Yang Y, Fu X, Zhang Y, et al. Gut microbial metabolite facilitates colorectal cancer development via ferroptosis inhibition. *Nat Cell Biol.* 2024;26:124–37.
38. Chen C, Wang Z, Jia S, Zhang Y, Ji S, Zhao Z, Kwok RTK, Lam JWY, Ding D, Shi Y, Tang BZ. Evoking highly immunogenic ferroptosis aided by Intramolecular Motion-Induced Photo-Hyperthermia for Cancer Therapy. *Adv Sci.* 2022;9:1–12.
39. Xie B, Zhao H, Ding YF, Wang Z, Gao C, Li S, Zhang K, Ip SW, Yu H, Wang R. Supramolecularly Engineered Conjugate of Bacteria and cell membrane-coated magnetic nanoparticles for enhanced ferroptosis and immunotherapy of tumors. *Adv Sci.* 2023;10:e2304407.
40. Zheng Y, Wang Y, Lu Z, Wan J, Jiang L, Song D, Wei C, Gao C, Shi G, Zhou J, et al. PGAM1 inhibition promotes HCC Ferroptosis and synergizes with Anti-PD-1 Immunotherapy. *Adv Sci.* 2023;10:e2301928.
41. Cui X, Lu G, Fang F, Xiong Y, Tian S, Wan Y, Xiao Y, Shen D, Wang H, Zhang J, Lee C-S. Iron Self-Boosting Polymer Nanoenzyme for low-temperature photothermal-enhanced ferrotherapy. *ACS Appl Mater Interfaces.* 2021;13:30274–83.
42. Zhou Y, Chen K, Lin WK, Liu J, Kang W, Zhang Y, Yang R, Jin L, Cheng Y, Xu A, Wang W. Photo-enhanced synergistic induction of ferroptosis for Anti-Cancer Immunotherapy. *Adv Healthc Mater.* 2023;12:e2300994.
43. Wu Q, Li Z, Zhou X, Wei Z, Ramadan S, Xu Y, Xu L, Li D. Photothermal Ferrotherapy - Induced Immunogenic Cell Death via Iron-based Ternary Chalcogenide nanoparticles against Triple-negative breast Cancer. *Small* 2023:e2306766.
44. Yuan H, Xia P, Sun X, Ma J, Xu X, Fu C, Zhou H, Guan Y, Li Z, Zhao S, et al. Photothermal Nanozymatic nanoparticles induce Ferroptosis and apoptosis through Tumor Microenvironment Manipulation for Cancer Therapy. *Small.* 2022;18:e2202161.
45. Luo L, Wang H, Tian W, Li X, Zhu Z, Huang R, Luo H. Targeting ferroptosis-based cancer therapy using nanomaterials: strategies and applications. *Theranostics.* 2021;11:9937–52.
46. Lan Y, Li X, Liu B, Lu J, Zuo B, Wang Y, Cao S, Fu X, Yue Q, Luo X, et al. Framework nucleic acid-based nanoparticles enhance temozolomide sensitivity in glioblastoma. *Drug Resist Update.* 2024;76:101122.
47. Guo R, Wang S, Zhao L, Zong Q, Li T, Ling G, Zhang P. Engineered nanomaterials for synergistic photo-immunotherapy. *Biomaterials* 2022, 282.
48. Cao D, Chen L, Zhang Z, Luo Y, Zhao L, Yuan C, Lu J, Liu X, Li J. Biodegradable nanomaterials for diagnosis and therapy of tumors. *J Mater Chem B.* 2023;11:1829–48.
49. Wang K, Shen R, Meng T, Hu F, Yuan H. Nano-Drug Delivery systems based on different targeting mechanisms in the targeted therapy of Colorectal Cancer. *Molecules.* 2022;27:2981.
50. Li L, He S, Liao B, Wang M, Lin H, Hu B, Lan X, Shu Z, Zhang C, Yu M, Zou Z. Orally Administrated Hydrogel Harnessing Intratumoral Microbiome and Microbiota-Related Immune responses for Potentiated Colorectal Cancer Treatment. *Research.* 2024;7:0364.
51. Zhang C, Yuan Y, Wu K, Wang Y, Zhu S, Shi J, Wang L, Li Q, Zuo X, Fan C, et al. Driving DNA Origami Assembly with a Terahertz Wave. *Nano Lett.* 2021;22:468–75.
52. Yu K, Chen Y, Zhang L, Zheng Y, Chen J, Wang Z, Yu X, Song K, Dong Y, Xiong F, et al. Cancer-Erythrocyte membrane-mimicking Fe₃O₄ nanoparticles and DHJS for Ferroptosis/Immunotherapy synergism in tumors. *ACS Appl Mater Interfaces.* 2023;15:44689–710.
53. Fan X, Yuan Z, Shou C, Fan G, Wang H, Gao F, Rui Y, Xu K, Yin P. cRGD-Conjugated Fe₃O₄@PDA-DOX multifunctional nanocomposites for MRI and Antitumor Chemo-Photothermal Therapy. *Int J Nanomed.* 2019;14:9631–45.
54. Liu M, Yu W, Zhang F, Liu T, Li K, Lin M, Wang Y, Zhao G, Jiang J. Fe₃O₄@Polydopamine-Labeled MSCs targeting the spinal cord to treat Neuropathic Pain under the Guidance of a magnetic field. *Int J Nanomed.* 2021;16:3275–92.
55. De Lorenzi F, Rizzo LY, Daware R, Motta A, Baues M, Bartneck M, Vogt M, van Zandvoort M, Kaps L, Hu Q, et al. Profiling target engagement and cellular uptake of cRGD-decorated clinical-stage core-crosslinked polymeric micelles. *Drug Deliv Transl Res.* 2023;13:1195–211.
56. Dasargyri A, Hervella P, Christiansen A, Proulx ST, Detmar M, Leroux JC. Findings questioning the involvement of Sigma-1 receptor in the uptake of anisamide-decorated particles. *J Control Release.* 2016;224:229–38.
57. Guo S, Li Z, Zhou R, Feng J, Huang L, Ren B, Zhu J, Huang Y, Wu G, Cai H, et al. MRI-Guided Tumor Therapy based on synergy of Ferroptosis, immunosuppression reversal and Disulfidoptosis. *Small.* 2024;20:e2309842.
58. Chen Y, Li H, Hou B, Wu A, Wu W, Li C, Wang H, Chen D, Wang X. NaYF₄:Yb/Er@Mn₃O₄@GOX nanocomposite for Upconversion Fluorescence Imaging and synergistic Cascade Cancer Therapy by apoptosis and Ferroptosis. *Small.* 2023;20:e2304438.

Publisher's note

Springer Nature remains neutral with regard to jurisdictional claims in published maps and institutional affiliations.